

PVF-10: A high-resolution unmanned aerial vehicle thermal infrared image dataset for fine-grained photovoltaic fault classification

Bo Wang^a, Qi Chen^{a,b}, Mengmeng Wang^{a,*}, Yuntian Chen^b, Zhengjia Zhang^a, Xiuguo Liu^a, Wei Gao^a, Yanzhen Zhang^a, Haoran Zhang^c

^a School of Geography and Information Engineering, China University of Geosciences (Wuhan), Wuhan 430074, China

^b Ningbo Institute of Digital Twin, Eastern Institute of Technology, Ningbo, 315200, China

^c School of Urban Planning and Design, Peking University, Shenzhen, 518055, China

HIGHLIGHTS

- A high-resolution and fine-grained PVF classification dataset (PVF-10) is proposed.
- The image features and circuit mechanisms of PVFs were comprehensively analyzed.
- Five SOTA models were employed to rigorously test PVF-10 as the benchmark.
- The CoaT-ls model achieved an OA of 93.32% for PVF classification on PVF-10.

ARTICLE INFO

Keywords:

Photovoltaic fault
Thermal infrared data
Classification
Deep learning
Unmanned aerial vehicle

ABSTRACT

Accurate identification of faulty photovoltaic (PV) modules is crucial for the effective operation and maintenance of PV systems. Deep learning (DL) algorithms exhibit promising potential for classifying PV fault (PVF) from thermal infrared (TIR) images captured by unmanned aerial vehicle (UAV), contingent upon the availability of extensive and high-quality labeled data. However, existing TIR PVF datasets are limited by low image resolution and incomplete coverage of fault types. This study proposes a high-resolution TIR PVF dataset with 10 classes, named PVF-10, comprising 5579 cropped images of PV panels collected from 8 PV power plants. These classes are further categorized into two groups according to the repairability of PVF, with 5 repairable and 5 irreparable classes each. Additionally, the circuit mechanisms underlying the TIR image features of typical PVF types are analyzed, supported by high-resolution images, thereby providing comprehensive information for PV operators. Finally, five state-of-the-art DL algorithms are trained and validated based on the PVF-10 dataset using three levels of resampling strategy. The results show that the overall accuracy (OA) of these algorithms exceeds 83%, with the highest OA reaching 93.32%. Moreover, the preprocessing procedure involving resampling and padding strategies are beneficial for improving PVF classification accuracy using PVF-10 datasets. The developed PVF-10 dataset is expected to stimulate further research and innovation in PVF classification.

1. Introduction

As a vital component of renewable energy, photovoltaic (PV) power generation has played a significant role in energy transition in recent years, experiencing widespread development globally [1,2]. The rapid construction of PV power plants on a global scale has led to an

impressive milestone by the end of 2022, with the total worldwide installed capacity of PV systems reaching 1183 gigawatts [3,4]. While new PV power stations continue to be developed, a considerable portion of existing facilities inevitably experience equipment aging over time. With the increase in operational duration, the probability of PV equipment faults also notably rises. These faults pose challenges to both the

Abbreviations: PV, Photovoltaic; PVF, Photovoltaic fault; TIR, Thermal infrared; UAV, Unmanned aerial vehicle; DL, Deep learning; CNN, Convolutional neural network; OA, Overall accuracy; Res-50, ResNet-50; Effv2-s, EfficientNet v2-small; ViT-s, Vision Transformer-small; Swinv2-t, Swin-Transformer v2-tiny; Coat-ls, Coat-lite small.

* Corresponding author.

E-mail address: wangmm@cug.edu.cn (M. Wang).

production efficiency and operational safety of the power stations [5,6].

One of the most typical challenges requiring effective management in PV operation and maintenance is the occurrence of various faults within PV modules [7]. Thermal infrared (TIR) imaging stands out as a prevalent technique utilized for detecting and analyzing these faults [8,9]. The underlying principle of TIR involves quantitatively sensing electromagnetic wave signals with wavelengths ranging from 6 to 15 μm [10]. Since the intensity of radiation emitted from the surface of an object within this wavelength range often correlates with the material and temperature of the object, the intensity values captured by the TIR sensor can be leveraged to accurately calculate the surface temperature of the object [11,12]. Due to alterations in the physical properties occurring inside or on the surface of the PV cell, the PV faults (PVFs) typically manifest as thermal anomalies on the TIR image, each exhibiting distinct characteristics [13–16].

Compared to handheld TIR cameras used for imaging PV panels, TIR imaging based on unmanned aerial vehicle (UAV) offers significantly higher data acquisition efficiency, particularly suitable for large-scale PV power plants [17]. Consequently, UAV-based TIR imaging has become an increasingly important tool for monitoring and diagnosing module faults in PV plant operation and maintenance [18,19]. The threshold segmentation and edge detection algorithms were early applied to detect PVF, by thresholding the grayscale values and detecting discontinuity in grayscale values of hot spots edge pixels [20–23]. However, these methods cannot classify PVFs. To classify the types of PVFs, researchers utilized machine learning algorithms with manual feature extraction. Feature extraction methods were employed to extract features from fault images, including the area or perimeter of PVF shape, gray-level co-occurrence matrix, and Histogram of Oriented Gradients (HOG) [24,25]. Based on these features, traditional machine learning algorithms like decision trees, K-Nearest Neighbors (KNN), and Support Vector Machines (SVM) are utilized to classify faults such as hot spots, overheated cells, and shading [14,26,27]. Compared with traditional machine learning models, deep learning (DL) models have the capability to automatically learn complex and abstract feature representations from raw data, thereby improving model performance and generalization ability [28,29]. Fine-tuning popular networks like VGG, ResNet, and MobileNet have achieved higher accuracy in PVF classification tasks [30,31]. Further, many researchers have proposed convolutional neural network (CNN)-based models for PVF classification to reduce model parameters and optimize computing costs [32–35]. DL algorithms have shown promising potential for classifying PVF from TIR images captured by UAVs, however, their performance relies on extensive and high-quality labeled data.

Many efforts have been taken to develop TIR image dataset for PVF classification. Based on open-source status, these datasets can be divided into two groups. Datasets in [36,37] are publicly available for open-source sharing, while the remaining datasets are not open-source, hindering replication and validation and impeding further research and innovation. According to the scale of the sample image, these datasets can be roughly grouped into three categories, including raw image-scale, submodule-scale (faults), and PV panel-scale datasets [38,39]. The submodule-scale and PV panel-scale datasets are constructed from raw images by image clip using the fixed size and PV panel boundary, respectively. However, the sample image contains multiple PV panels in raw image-scale datasets, and submodule-scale datasets contain incomplete PV panels, hindering their application in PVF classification defined at single PV panels. In addition, datasets in [37,40,41] suffer from insufficient number of samples and incomplete coverage of fault types, limiting the generalization and practical utility of the model trained by these datasets. Besides, the spatial resolution of datasets in [41–43] are lower than 0.03 m and cannot provide detailed spatial information to discern characteristics difference between varied PVFs. The existing datasets cannot simultaneously meet the requirements of high spatial resolution, PV panel scale, and sufficient number and fault types. In addition, few existing studies have analyzed the circuit mechanism

behind the image features of PVF.

To address these research gaps, this study develops an open-source UAV TIR image dataset, named PVF-10, to facilitate the advancement of fine-grained UAV-based PVF classification. We first determined the data acquisition requirements, including weather conditions, irradiance, wind speed, temperature, humidity, and flight altitude, based on the acquisition conditions permitted by the TIR sensor and UAV, and to ensure clear discernibility of PVFs on the TIR images. Then, we employed experts to precisely annotate and classify defective PV panels in the TIR images. These panels were then cropped into separate images, enabling the training of models specifically designed for PVF classification. Lastly, we utilized several state-of-the-art DL models to train and test the PVF-10 dataset, aiming to provide a benchmark for assessing the performance of PVF classification algorithms. Our main contributions are as follows:

- 1) A high-resolution PVF TIR image dataset is developed. Compared to existing research, it is currently the highest spatial resolution open-source dataset for classifying PVFs, which is instrumental in advancing fine-grained PVF diagnosis techniques.
- 2) Leveraging high-resolution imaging capabilities, we comprehensively analyze the relationship between TIR image features of PVFs and the circuit principle of PV panel, which enhances our understanding of the mechanisms behind the hot spot formation of PVFs.
- 3) We evaluated state-of-the-art DL-based image classification models in the context of PVF classification, while also analyzing the impact of image sampling strategies on classification accuracy, which can serve as baselines for future PVF classification.

The organization of this paper is as follows: Section 2 introduces the framework for PVF-10 dataset construction. Section 3 tests and evaluates the PVF-10 dataset using five prevalent DL models. Finally, the limitations and implications of this work are summarized in Section 4.

2. Dataset construction

The framework of the PVF-10 dataset construction involves four parts, including: 1) Acquisition of raw TIR image and data preprocessing, 2) Design of the PVF classification system considering the cause and repairability of the PVF, 3) Analysis of circuit mechanisms underlying image features of PVF, and 4) Labeling of PVF samples, as illustrated in Fig.1.

2.1. TIR image acquisition and data preprocessing

To acquire high-quality TIR PVF samples, we employed UAVs equipped with TIR sensors (DJI H20T&M30T) to capture images from eight PV power plants. These plants involve four typical PV application scenarios (see Fig. 2), facilitating the acquiring more comprehensive and varied PV module types. In total, 109,244 TIR images as well as corresponding visible images were collected to enhance the screening of fault photos and the annotation of fault samples. The data collection procedure comprised the following steps: surveying the field area, planning flight routes and parameters based on the weather and environmental conditions of the power station, and implementing the data acquisition plan under conditions meeting criteria such as irradiance and temperature.

The main factors influencing the image quality are meteorological conditions and the spatial resolution of the images. Data collection was conducted under clear skies with solar irradiance exceeding 500 W/m² and wind speeds of less than 10 m/s. Meteorological parameters during the data collection period were recorded, including temperature, humidity, wind speed, and solar radiation, as shown in Table I. Flight altitude directly impacts the spatial resolution of the image. With increasing flight altitude, there is an improvement in data acquisition efficiency, but a simultaneous reduction in data quality. Therefore, a

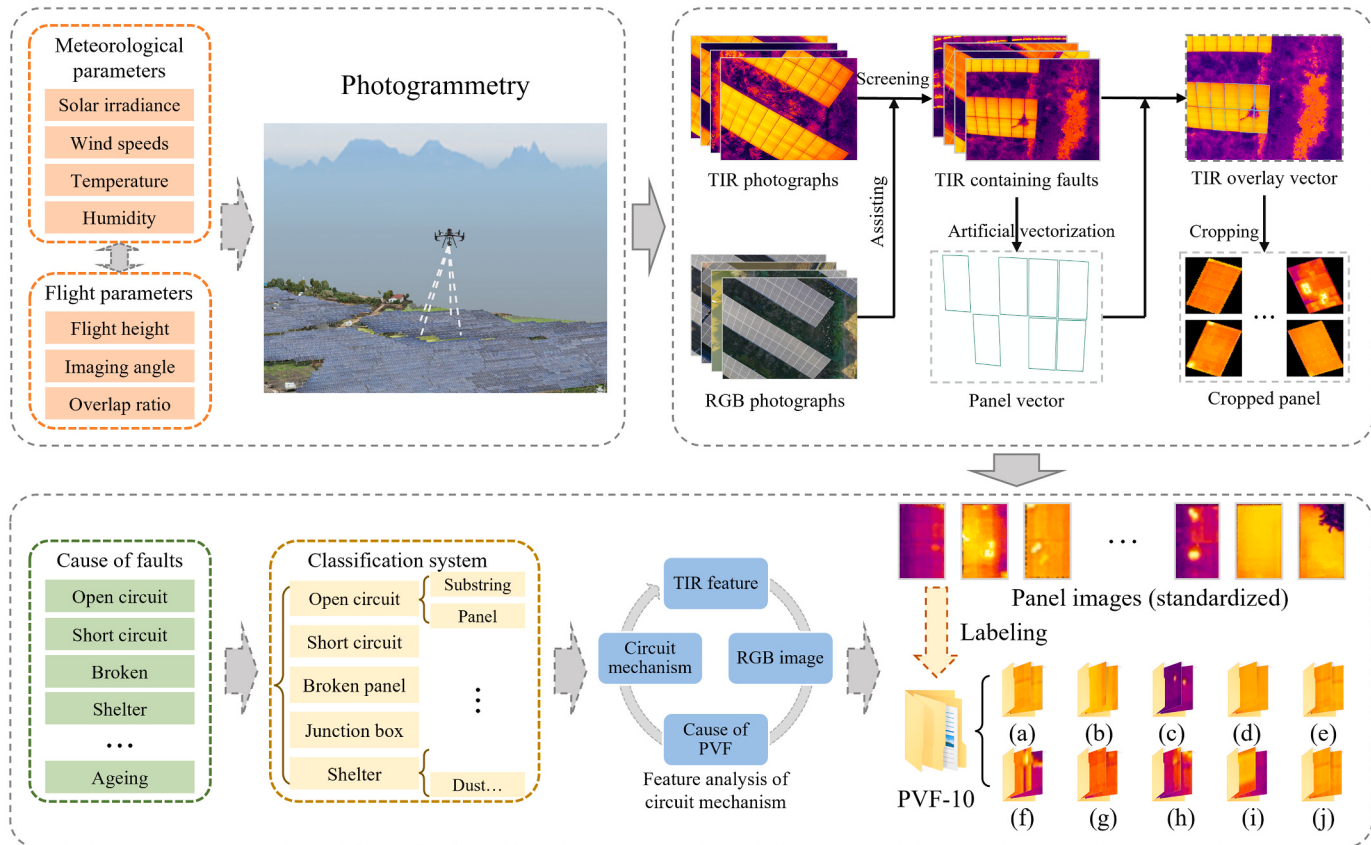


Fig. 1. The framework for generating PVF-10 dataset, including TIR image acquisition and data preprocessing, PVF classification system construction, and labeling annotation.

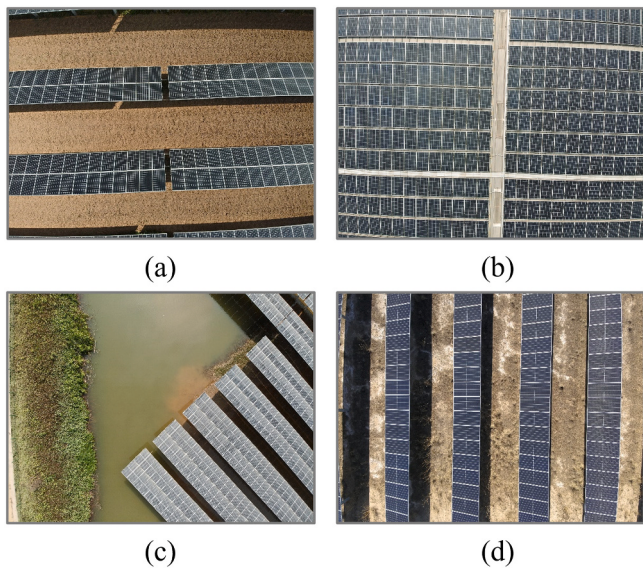


Fig. 2. Types of PV application scenarios: (a) Agricultural and PV, (b) Rooftop-distributed PV, (c) Fishery PV, and (d) Centralized PV.

comparative experiment of data collection at different altitudes was conducted to assess the impact of spatial resolution on imaging quality, as detailed in the supplementary materials. Based on the comparative experiment, the flight altitude was determined to be 20 m, capturing images with spatial resolutions between 1.8 and 2 cm, which can meet the requirement of PVF classification. Additionally, the imaging angle of

the sensor was fixed at 90°.

The data preprocessing procedure for generating sample images involved two steps: screening TIR images with the quality criteria and cropping TIR images using PV panel boundary, as illustrated in Fig. 1. Firstly, with the assistance of RGB images, TIR images containing fault panels with distinct edges and no significant perspective distortion were selected. Subsequently, artificial vectorization was employed to delineate the outline vectors of faulty PV panels in the raw TIR images. Meanwhile, outline vectors for negative samples (healthy panels) were randomly sketched. The raw TIR images were cropped into individual PV panel images using the outline vectors of the panels.

2.2. PVF classification system construction

According to the IEC TS 62446–3 international standard, PVFs were classified into ten categories: (a) modules in open, (b) modules in short, (c) crystalline module with broken front glass, (d) substring in short circuit, (e) 1 × substring in open circuit, (f) 2 × substrings in open circuit, (g) single cell with difference in temperature, (h) module with cells shaded by dirt, (i) transfer resistance at cell connections of a crystalline module, (j) heated module junction box [44]. Among, both (e) 1 × substrings in open circuit and (f) 2 × substrings in open circuit are substring open circuit; (i) transfer resistors at the cell connections of crystalline assemblies and (j) heated assembly junction boxes are shown on the junction box overheating; and the cell obscured by dirt, such as bird droppings or leaves, etc. lead (h) module with cells shaded by dirt. On this basis, a new classification system was proposed, combining (e) 1 × substring in an open circuit and (f) 2 × substrings in the open circuit as substring open circuit, determining (i) transfer resistance at the cell connection of the crystal module and (j) heated module junction box as junction box heating, adding fault categories of dust band and shadowed

Table I

Data acquisition details for the selected power plants, including measurements of wind speed, irradiance, temperature, and humidity.

Name	Province	Type*	Sensor	Image number	Wind speed (m/s)	Irradiance (W/m ²)	Temperature (°C)	Humidity (%)
Taiqian huadian	Henan	A	DJI H20T	13,199	5.7–5.9	225.4–927.0	24.5–27.6	42.9–52.5
Huanggang chencelou	Hebei	A	DJI M30T	2376	3.6–4.2	174.9–200.7	15.5–15.8	77.5–79.1
Baiyun electric equipment	Guangdong	B	DJI H20T	7586	0.7–1.6	147.6–871.5	18.5–22.1	35.8–46.3
Nanyang cable	Guangdong	B	DJI H20T	6116	0.1–0.7	369.8–868.6	18.7–23.6	40.0–42.1
Liuhe machine	Guangdong	B	DJI H20T	4390	1.2–1.6	325.1–806.7	22.6–23.7	38.1–43.4
Shuangyi latex	Guangdong	B	DJI H20T	4849	0.2–0.6	541.0–804.4	18.7–23.1	50.0–65.4
Wencun photovoltaic	Guangdong	C	DJI H20T	56,328	1.9–3.1	246.9–674.7	20.3–20.8	96.1–88.6
Hongqi power plant	Qinghai	D	DJI M30T	14,400	2.0–2.5	535.4–639.0	1.5–8.0	21.6–32.2

* The type of PV application scenarios: A (Agricultural and PV), B (Rooftop-distributed PV), C (Fishery PV), and D (Centralized PV).

panel. In addition, the PVFs were grouped considering the causes and repairability of the fault to provide specific information support for PV operation and maintenance.

- 1) *Causes of PVFs:* As depicted on the left side of Fig. 3, the causes of PVFs include either the damage of the internal electronics and circuits of the PV panel or external environmental factors. Circuit anomalies encompass open circuits (such as substring open circuit and panel open circuit), short circuits (including substring short circuit and panel short circuit), junction box heating, and battery overheating. The external environment that causes PVFs consist of the broken panel and shelter. Further, shelter can be categorized into debris coverage, shadowed panel, and dust panel bottom.
- 2) *Repairability of PVFs:* As shown on the right side of Fig. 3, according to the repairability of PVFs, the ten types of PVFs were classified into two categories: reparable and irreparable PVFs. Reparable PVFs can be restored by removing the shelter or reconnecting the external circuit of PV modules, such as the shelter, panel open circuit, and panel short circuit. Irreparable PVFs require the replacement of the PV panel or encapsulated electronic components, including substring open circuit, substring short circuit, broken panel, junction box heating, and overheating cell. For instance, the broken panel

necessitates replacing the entire PV panel. Additionally, if the fault of cell overheating impacts the power generation of the entire string, replacement of the PV panel becomes necessary.

2.3. Image feature and circuit mechanism analysis of PVFs

To comprehensively understand the classification system of PVFs, the image feature and its underlying circuit mechanisms of PVFs were analyzed with the assistance of visible images and circuit diagrams of PV panels (see Fig. 4). As fundamental power-generating units in a PV panel, cells are PV conversion elements made from silicon semiconductors. Cells are typically organized into six rows, with each adjacent two rows connected in series to form a substring. The junction box that consists of connecting wires and the bypass diode is the electrical power output device of the PV panel. The bypass diode is configured in parallel with the PV panel's substring and its primary role is to initiate conduction when the sub-string exhibits excessive internal resistance or an open-circuit condition. Analysis of image features and circuit mechanisms for each PVF is presented in the following.

- 1) *substring open circuit:* Fig. 5 (a) shows the image of a substring open circuit. As shown in the circuit diagram, each substring of

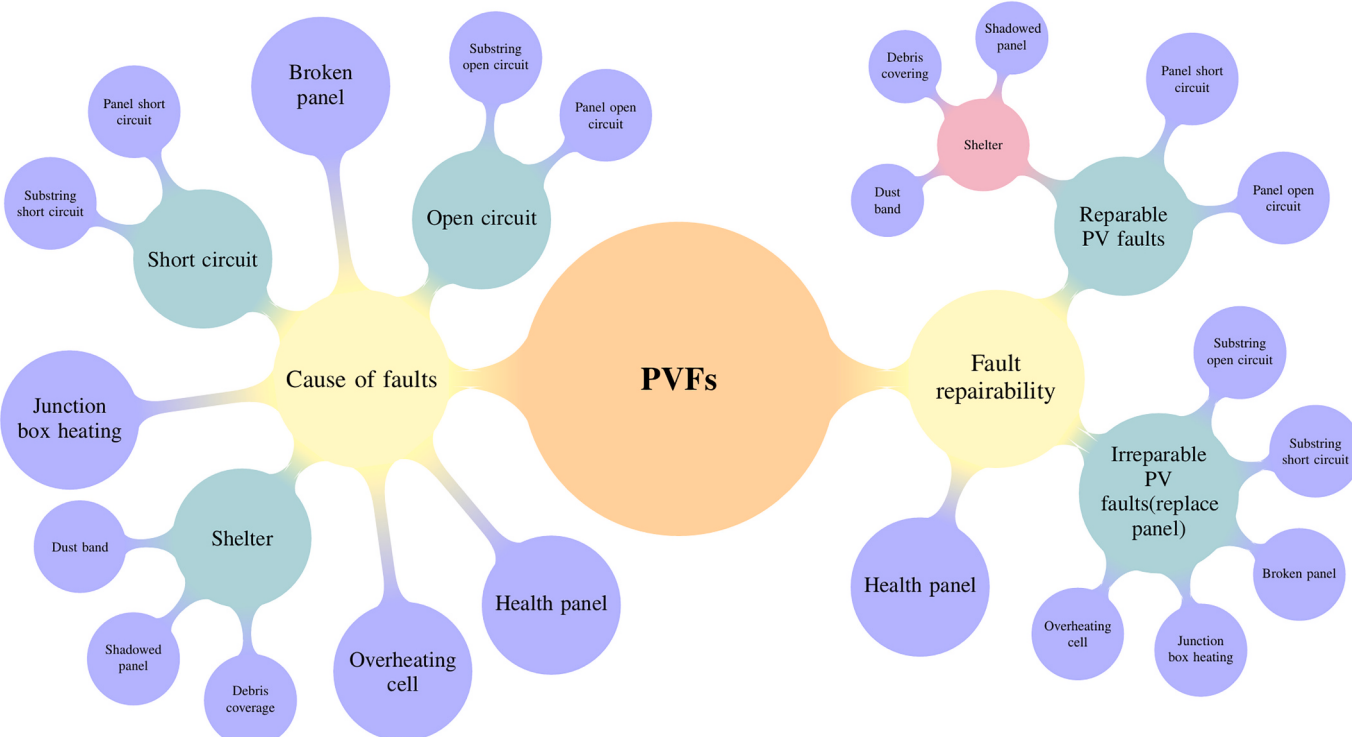


Fig. 3. PVF classification system based on the causes (left) and repairability (right) of faults.

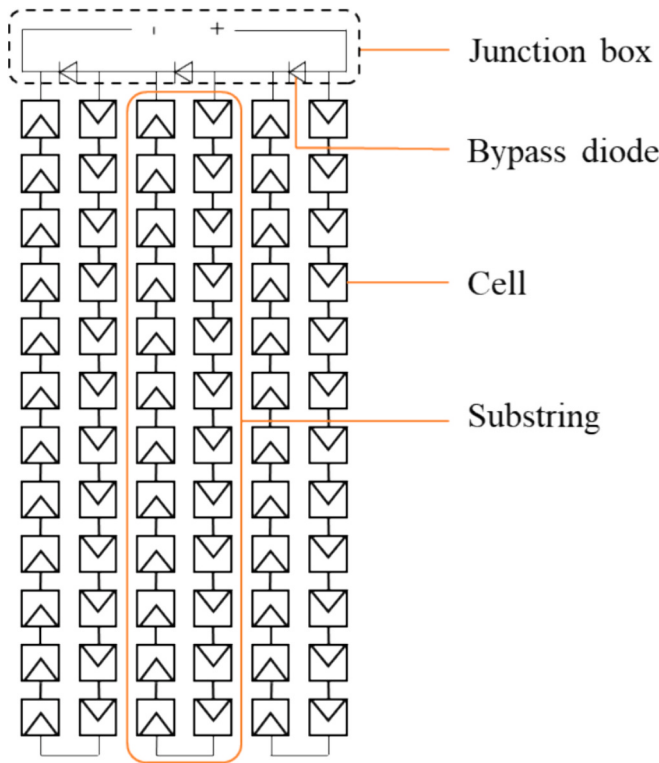


Fig. 4. Circuit diagram of a PV panel.

the PV panel is paralleled with a bypass diode, which is activated when the internal resistance of the substring is too high or the substring is internally disconnected [45]. Consequently, the affected substring stops functioning, and the unconverted light energy is converted into heat energy. The temperature of the disconnected substring area increases compared to the area of normal power generation. This distinct temperature anomaly is clearly observable in TIR images, where one or two substring regions exhibit higher temperatures than the normal ones. Fig. 5 (1) shows the RGB image of the substring open circuit, which is indiscernible through the RGB image. However, the substring open circuit fault will be brighter than other normally operating substrings in the TIR image and can lead to the power loss of one-third or two-thirds of the panel.

2) *Panel short circuit:* Fig. 5 (b) and (2) display the image of the panel short circuit. Panel short circuit occurs when the positive and negative poles of the PV panel are directly connected. When the panel short circuit occurs, the individual cells within the PV panel suffer varying effects, attributable to the differential voltage of the cells' terminals [46]. When the cell's voltage exceeds the average voltage in the circuit, it normally operates and generates electrical energy, as indicated by the gray cells in Fig. 5 (b). Conversely, when a cell's voltage is below the circuit's average voltage, it consumes electrical energy, as represented by the red cells in Fig. 5 (b). The electrical energy consumed by the cells is released into the environment in the form of heat and long-wave radiation, thus causing the short-circuited panel to show numerous unevenly distributed overheated cells. In addition, since electroluminescence is invisible light, the panel short circuits are invisible faults in visible light images [47].

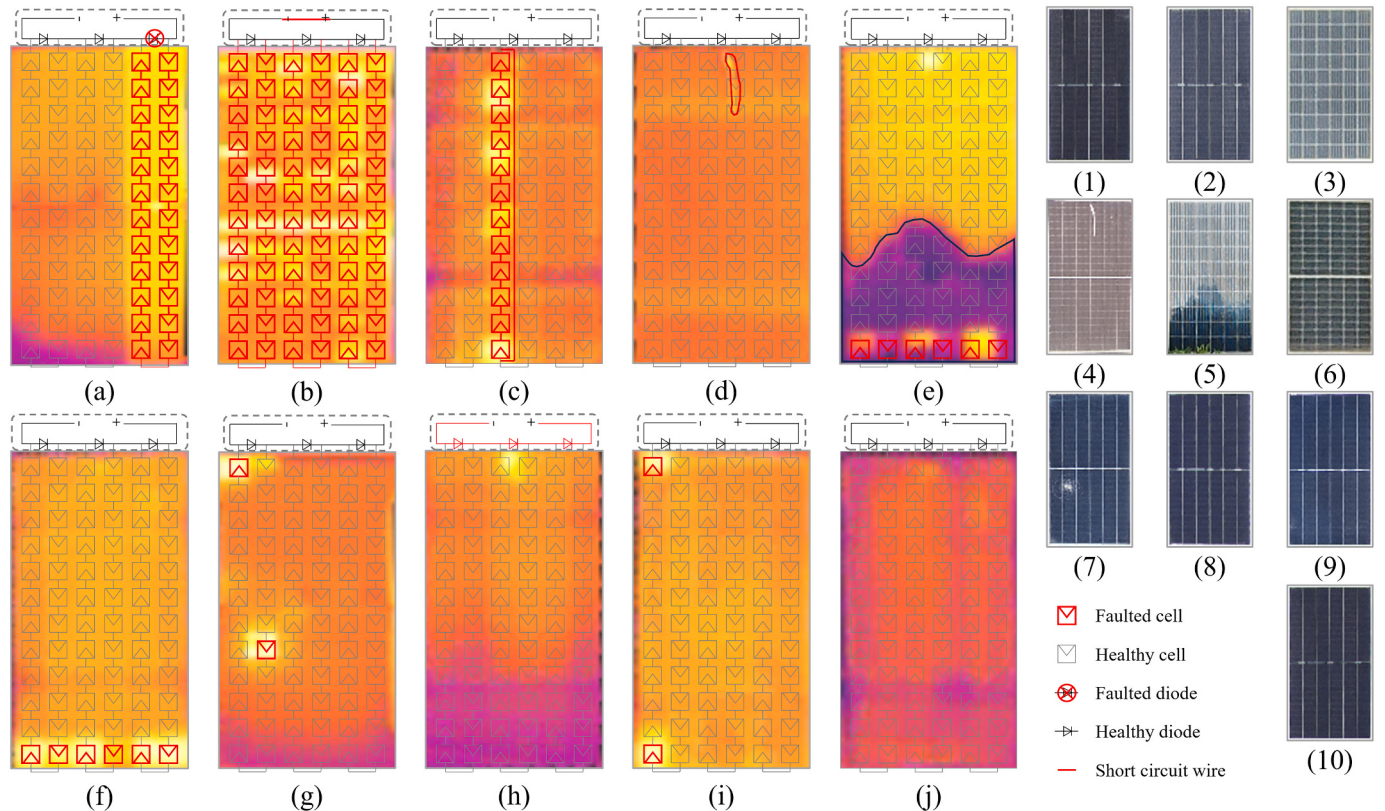


Fig. 5. TIR images and RGB images of various fault types: (a) substring open circuit, (b) panel short circuit, (c) substring short circuit, (d) debris covering, (e) shadowed panel, (f) dust band, (g) broken panel, (h) junction box overheating, (i) overheated cell, (j) healthy panel; (1) substring open circuit, (2) panel short circuit, (3) substring short circuit, (4) debris covering, (5) shadowed panel, (6) dust band, (7) broken panel, (8) junction box overheating, (9) overheated cell, (10) healthy panel.

- 3) *Substring short circuit*: Fig. 5 (c) and (3) display the images of the substring short circuit. Substring and panel short circuits have similar appearances in the TIR images, and neither can be detected in visible light images. The circuit diagram illustrates that substring short circuits in the PV panel are caused by short circuits within the substring and a current circuit is formed within this substring. As similar with panel short-circuit, the disparity in cell voltages within the short circuit results in cells in the substring simultaneously generating and discharging power from the cells in the substring, leading to irregularly heated cells in the TIR image of the shorted substring area.
- 4) *Debris covering*: Fig. 5 (d) displays debris coverage on the panel. Debris refers to elements like leaves, bird droppings, mud spots, and other minute particles on the surface of the PV panel's glass. These debris, which are clearly recognizable in visible light images, cover the surface of the PV panels, reducing their power generation, as shown in Fig. 5 (4). Due to the different thermal conductivity of the debris compared to the panel glass, the temperature in the debris-covered areas will also be different from the other areas, resulting in bright or dark spots on TIR images.
- 5) *Shadowed panel*: Fig. 5 (e) and (5) display images of shadowed panels. These panels are characterized by long-term shadowing of portions of their surfaces, which is usually caused by large structures or vegetation that blocks sunlight, such as vegetation that grows in large numbers attached to the surface of the panels. This phenomenon is evident in visible light photographs, where a portion of the panel's surface appears shaded. Due to the absence of solar radiation, the temperature of the shaded area is lower compared to sun-exposed areas on the PV panel. Notably, some cells within these shadowed areas generate heat due to electrical current passing through them. Consequently, TIR images of the shadowed panel reveal cold-shadowed regions and overheated cells, as shown in Fig. 5 (e).
- 6) *Dust band*: Fig. 5 (f) displays the fault that is called the dust band, which occurs because PV panels are typically installed at an angle, allowing rainwater to transport dust on the PV panel to accumulate at the bottom of the panels. As the water evaporates, it leaves behind a concentrated area of dust at the bottom of the panel, forming what is known as the dust band. The dust band is clearly visible at the bottom of the PV panel in the visible light image of Fig. 5 (6). Similar to shadowed panels, cells under the dust band cannot generate electricity. When current flows through them, the temperature of cells becomes high. Prolonged exposure to high temperatures can cause irreversible degradation to the cells at the bottom of the panel, adversely impacting the overall power generation efficiency of the PV panel.
- 7) *Broken panel*: The broken panel refers to the fracturing of surface glass and internal cells of PV panels, which occurs due to external pressure or object impact. As shown in Fig. 5 (7), The radial texture of the broken panel glass is readily identifiable in the visible light image. As shown in Fig. 5 (g), the broken panel may cause two types of faults: (1) Changes in the surface glass transmittance hinder the cells' ability to generate electricity normally, leading to heating as current flows through them; (2) Excessive force can cause cracks of cells, which in turn leads to heating [48]. Under the influence of the broken glass's texture, the radial pattern is also evident in the TIR image.
- 8) *Junction box overheating*: Fig. 5 (h) illustrates the overheating junction box, a condition caused by either corroded wiring within the box or poor contact due to substandard soldering. This inadequate contact leads to arcing inside the junction box, elevating its temperature. In extreme cases, this can result in the junction box burning out [49]. The TIR image shows that the temperature in the junction box area is higher than in the other locations. Different models of PV panels across various power plants lead to varying installation locations for the junction boxes. From Fig. 5 (h), there is only one junction box for the PV panels in the first three TIR sample images, and two junction boxes on the centerline of the PV panels in the last two TIR sample images. Junction box overheating remains invisible on visible light images, as shown in Fig. 5 (8).
- 9) *Overheated cell*: Individual cell cracks or aging generally cause the fault of the cell overheating, which is the most common fault in PV modules. The reason for the cell cracks or aging can cause less current and voltage than the normal cells, and current backflow causes the cell to heat up [49]. As shown in Fig. 5 (i), one or more cells may be overheating in a panel, but unlike string opens and shorts, overheated cells do not appear in series but randomly distribute across the PV panel. Cell overheating is shown on the TIR PV panel images as one or more cell-shaped (rectangular) hot spots.
- 10) *Healthy panel*: All components within the healthy panel operate optimally and without any overheating so that the panel shows a relatively uniform surface temperature on the TIR image. However, it is important to note that the non-flat of the PV panel surface can influence pixel value in the TIR image, leading to the temperature on the panel is not a unique value (generally fluctuating by 0.5 °C). As shown in Fig. 5 (j), due to the non-flat surface of the PV panel, the purple low-temperature area on the third TIR image is a normal condition.
- 11) *Panel open circuit*: The panel open circuit signifies its disconnection from the external circuit, in which case all cells within the PV panel are inoperative, and unused solar radiation is released into the environment in the form of heat. Similar to the substring open circuit, the surface temperature of the panel is higher than the healthy panel. However, since the sample images of the dataset are RGB pseudo-color images rendered from a single-channel image of the temperature, both healthy panels and open-circuit panels show uniform temperature values. To distinguish between open circuit panels, it is necessary to compare the temperature values with those of other panels, which can't be classified from the image of the individual PV panel. Thus, the panel open circuit is not included in PVF-10.

2.4. Labeling annotation

During the PVF type annotating process, it is inevitable that errors from category ambiguities or labeling experts' carelessness. To ensure consistent labels of PVF samples, we implemented a dual labeling comparison strategy for verification. Initially, two experts independently labeled the types of PVFs. Subsequently, labels of the same sample labeled two experts are compared for consistency. If the labels are consistent, it is confirmed. In instances of inconsistency, the experts engage in discussions to reconcile these discrepancies and establish labels of PVFs. After strict category labeling and sample normalization, the size of the PVF-10 and the number of samples in each category are determined. Fig. 6 shows a randomly selected example of each type of fault. There are 5579 samples in the PVF-10, of which the number of samples in each category is shown in Fig. 7.

3. Experiment and discussion

This section presents classification experiments based on PVF-10 using deep neural network models to demonstrate the usability of the PVF dataset and evaluate the performance of various classification models.

3.1. Implementation details

To ensure a fair comparison, the selected models, including ResNet (Res-50), EfficientNetV2 (Effv2-s), Vision Transformer (ViT-s), Swin Transformer V2 (Swinv2-t), and Coat (Coat-ls), have similar parameter

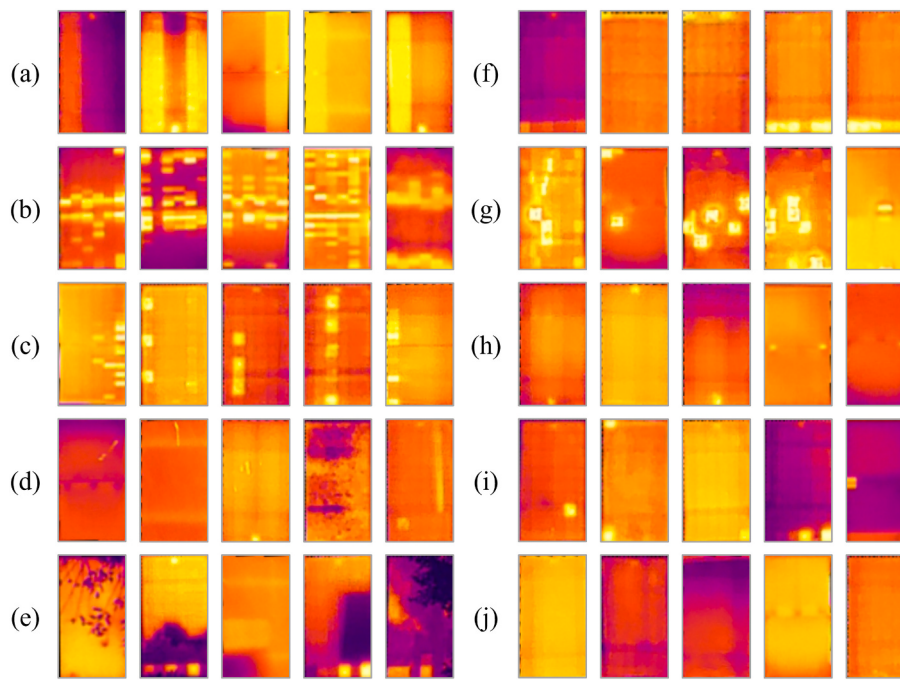


Fig. 6. Pseudo-color TIR images of PVF: (a) substring open circuit, (b) panel short circuit, (c) substring short circuit, (d) debris covering, (e) shadowed panel, (f) dust band, (g) broken panel, (h) junction box overheating, (i) overheated cell, (j) healthy panel.

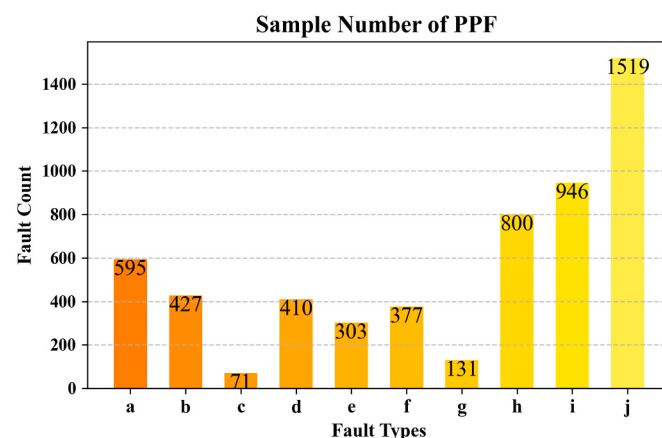


Fig. 7. Distribution of sample counts in PVF-10 dataset for various fault types: (a) substring open circuit, (b) panel short circuit, (c) substring short circuit, (d) debris covering, (e) shadowed panel, (f) dust band, (g) broken panel, (h) junction box overheating, (i) overheated cell, (j) healthy panel.

counts, and their algorithm block diagram are detailed in supplementary materials [50–54]. These models were trained using the PyTorch framework on an NVIDIA GEFORCE RTX 4080 16G. The widely used AdamW was employed as the optimizer with β_1 of 0.9 and β_2 of 0.999. Through several experiments, we determined the optimal learning rate for each model, as detailed in Table II. We adopt the learning rate scheduling strategy of cosine annealing, which cyclically fluctuates the learning rate in a cosine curve pattern to prevent the loss from getting stuck in local minima. To mitigate the impact of batch size differences in experiments, the batch size was set to 32 for all models. The cross-entropy loss is utilized as loss function for all models. All models were trained for 300 epochs without loading pre-trained weights, achieving convergence of the loss. To prevent overfitting, data augmentation techniques such as random flipping and 90° rotations were applied during image loading. Additionally, the samples were resized to 224 × 224 pixels before being input into the model.

To standardize samples, we employed the following resampling strategy: After the image preprocessing, TIR images were cropped as individual PV panel images, as shown in Fig. 8 (a). Through investigating the dimensions of PV panels in different power plants, we found that the aspect ratio of the panels ranges from 1.7 to 2.1. The individual PV panel images have dimensions ranging from 120 to 100 pixels in length and 63 to 55 pixels in width. Therefore, to maintain the original proportions of the sample images, the sizes of the sample images were specified as 110 × 60, as shown in Fig. 8 (b). Considering the impact of input dimensions of most classification models on the original panel shape, leading to differences in classification results, we performed padding to the sample images of size 110 × 60 by surrounding them with zeros, resulting in a size of 112 × 112, as depicted in Fig. 8 (c). Finally, we randomly partitioned the dataset into training, validation, and test sets according to the proportions of each type, with 90% allocated for training and validating, and 10% for testing, as a default sample split.

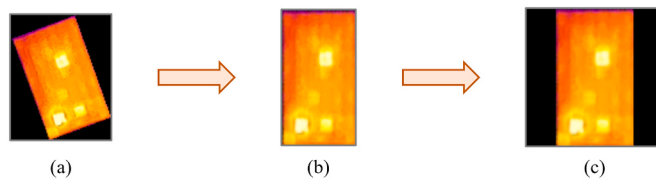
3.2. Overall comparison between different DL models

Table II displays the classification evaluation index of the models on the test set, including overall accuracy (OA), precision, recall, and F1 score. The results indicate that all models achieved classification OA exceeding 83% on PVF-10, suggesting good discriminative capability among samples of different types in PVF-10. Res-50 achieved an OA of 92.42%. Notably, the OA of Effv2-s and Coat-ls exceeded 93%. However, ViT-s, which performed well on ImageNet, achieved a classification OA of only 83.57% in PVF classification, which might be due to the absence of pre-trained weights during model training, leading to suboptimal performance of the Transformer model in the context of limited number of samples. Similarly, the OA of Swinv2-t was 89.71%, which was lower than that of CNN architectures. Therefore, we observed that the classification OA ranking of different architectures was as follows: CNN + Transformer (Coat) > CNN (ResNet, EfficientNet) > Transformer (SwinV2, ViT). However, EfficientNet demonstrated the highest precision, recall, and F1 score, indicating its superior performance, possibly due to its effectiveness in handling imbalanced sample sizes.

Table II

Comparison of results from different resample strategies and models.

Resampling strategy	Model	Parameters	Learning rate	Fps (items/s)	OA (%)	Precision	Recall	F1 score
Original panel image	Res-50	23.5 M	0.0005	17.50	91.52	0.8827	0.8686	0.8684
	Effv2-s	20.3 M	0.0005	15.81	90.79	0.8653	0.8690	0.8650
	ViT-s	22.5 M	0.0002	16.07	76.89	0.6867	0.6722	0.6773
	Swinv2-t	21.1 M	0.0005	15.25	89.16	0.8795	0.8243	0.8456
	Coat-ls	20.2 M	0.0002	17.80	90.97	0.9183	0.8341	0.8666
Resampled panel image (110 × 60)	Res-50	23.5 M	0.0005	17.10	91.15	0.9168	0.8843	0.8981
	Effv2-s	20.3 M	0.0005	16.99	92.42	0.9201	0.9068	0.9090
	ViT-s	22.5 M	0.0002	15.64	81.27	0.7556	0.7369	0.7444
	Swinv2-t	21.1 M	0.0005	14.98	90.61	0.9060	0.8717	0.8834
	Coat-ls	20.2 M	0.0002	16.21	91.69	0.9188	0.8698	0.8913
Resampled and padded panel image (112 × 112)	Res-50	23.5 M	0.0005	17.95	92.42	0.8978	0.8902	0.8934
	Effv2-s	20.3 M	0.0005	16.12	93.14	0.9133	0.8986	0.9038
	ViT-s	22.5 M	0.0002	16.98	83.57	0.7836	0.7629	0.7706
	Swinv2-t	21.1 M	0.0005	13.87	89.71	0.8585	0.8453	0.8505
	Coat-ls	20.2 M	0.0002	14.06	93.32	0.9095	0.8746	0.8874

**Fig. 8.** Sample image after different level of preprocessing. (a) original panel image, (b) resampled panel image (110 × 60), (c) resampled and padded panel image (112 × 112)

3.3. The classification performance of diverse fault types

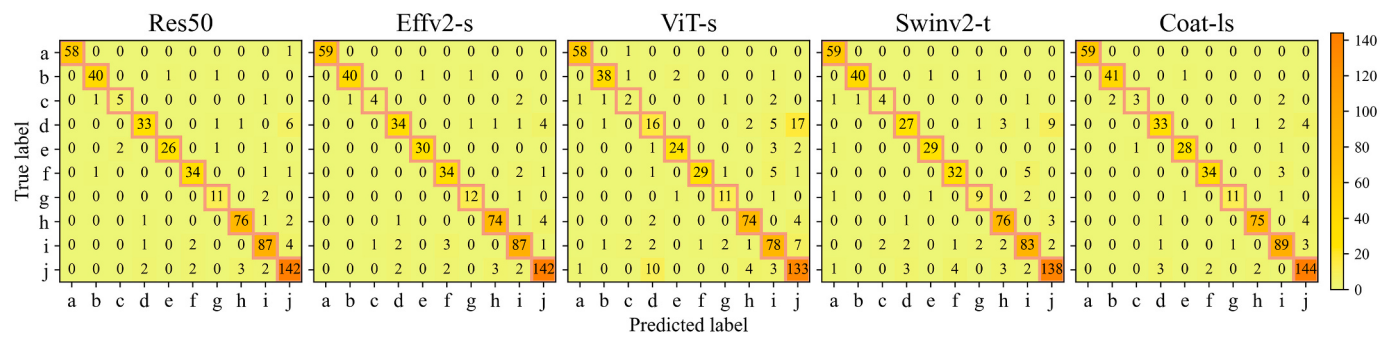
Confusion matrices are employed to illustrate the relationship between the predicted labels generated by the models and the truth labels, providing a more detailed understanding of the performance of different models on diverse PVF types, as depicted in Fig. 9. Res-50 and Effv2-s achieve similar accuracies, but Effv2-s demonstrates slightly stronger overall performance. For instance, Effv2-s achieves 100% accuracy on healthy panels in (a) and (e), while Res-50 exhibits misclassification. Compared to other models, ViT-s performs poorly on PVF-10 due to its low accuracy on (c), (e), and (j). In particular, its recognition ability is relatively weak in the (c) and (j), as demonstrated by the fact that many instances of (c) are incorrectly categorized as (j), while many instances of (j) are classified into the (c), which may be because ViT-s loses the features of (c) in its prediction. Notably, ViT-s and Swinv2-s are not as accurate as the other models on (c) and (d), primarily because CNNs have a superior ability to extract texture features compared to Transformers. However, several samples exhibit misclassifications across most models. For example, portions of (d) were erroneously classified as class (j), likely due to temperature fluctuations in these images caused by sensor noise or artifacts. Similarly, some samples labeled as (h) were

misclassified as (j), possibly because of small debris on the PV panels, interpreted by the models as noise in an otherwise healthy sample. In addition, several instances of (j) were misclassified as (d), possibly stemming from our classification criteria based on temperature images, where a temperature difference greater than 3 °C between the junction box and the healthy panel is considered a fault. However, the models may struggle to detect such temperature differences in pseudo-colored images.

Based on above analysis, it is concluded that different models show different performance on diverse fault types due to their shape features of faults, distribution features of high-temperature region. The large convolution kernels have a larger receptive field and are more effective at extracting shape features, while small convolution kernels are more beneficial for extracting texture features [55]. Considering the large receptive field advantage of Transformers, the global distribution characteristics of high-temperature regions can be effectively extracted [53]. Therefore, future algorithms should consider combining the advantages of small-size convolutional kernels (texture features) and large-size convolutional kernels (shape features) or integrating the capabilities of convolutional networks (texture and shape features) with Transformers (global distribution features) to design.

3.4. The impact of resampling strategy on PVF classification

As shown in Table II and Fig. 10, sampling strategies have an impact on model performance. The performance of five models shows improvement from the original panel image to the resampled panel image, and further to the resampled and padded panel image. This finding suggests that resampling and padding strategies can aid the model in understanding the image features of the PVF samples. The perspective distortion caused by the installation angle of PV components and lens distortion affects the original sample images, further negatively

**Fig. 9.** Confusion matrices of the model for resampled and padded image (112 × 112).

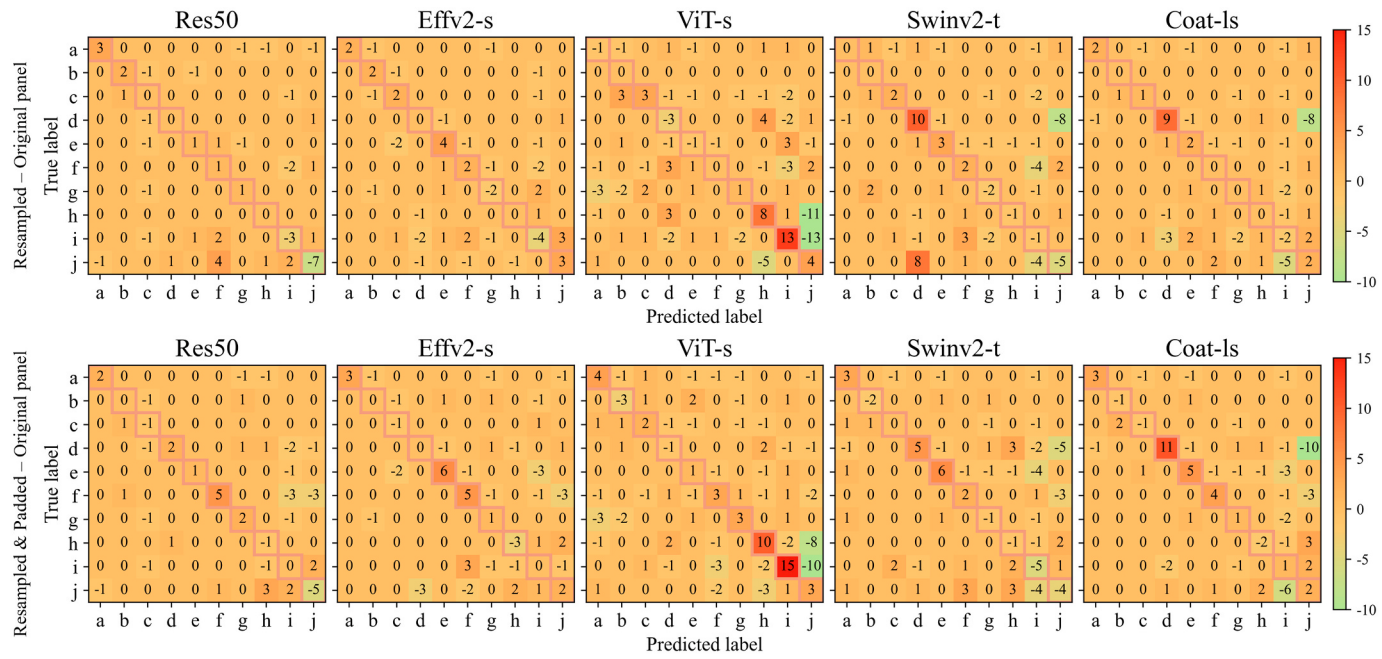


Fig. 10. The confusion matrix difference obtained by subtracting the confusion matrix of the original panel image (110×60) and the resampled and padded panel image (112×112).

impacting the algorithm's recognition accuracy for some PVF types. In particular, there is a significant improvement in accuracy for (a), (d), (e), and (f) after resampling and padding compared to the original samples. This improvement is likely due to the restoration of hot spots original shape through resampling and padding. Thus, it is evident that the model's recognition of (a), (d), (e), and (f) relies more on the shape features of the faults. Conversely, the recognition of (b), (c), (h), and (i) relies more on the distribution features of thermal anomalies on the panels.

4. Conclusion

This study has constructed an open-source UAV TIR image dataset named PVF-10, comprising 5579 cropped images of PV panels collected from 8 plants and categorized into 10 different categories. Notably, the spatial resolution of the PVF-10 dataset reaches 0.02 m , providing an equivalent of approximately 60×110 effective pixels for imaging a $1.2 \times 1.7\text{ m}$ PV panel. Image features and their underlying electrical mechanisms for each PVF were analyzed based on visible images and circuit diagrams of PVF. These analyses not only deepen our understanding of the mechanisms causing heat spots on PV panels but also offer valuable insights for PV operators in maintaining PV power generation systems.

To our knowledge, the proposed dataset is currently the highest spatial resolution and open-source TIR dataset for PVF classification. However, PVF-10 still has two limitations: 1) sample quantity: Despite the considerable sample quantity of PVF-10, 5579 samples are still insufficient for models with larger parameters. In our experiments, the OA of ViT and Swin-Transformer are lower than that of CNN models, due to the self-attention mechanisms in Transformers require more training data than CNN. 2) sample imbalance: The quantities of (c) shadowed panel and (g) broken panel are less than that of other types. The imbalanced sample distribution can cause the model's predictions to be biased towards the more abundant sample types. In future work, we plan to utilize a strategy for updating the dataset to improve sample quantity and imbalance.

Five state-of-the-art DL algorithms were trained and validated on the PVF-10 dataset using three levels of resampling strategy. Among them,

the Coat, which combines CNN and Transformer architectures, achieved an impressive OA of 93.32%. These model results establish valuable baselines for the development of future algorithms. In future work, more accurate classification algorithms tailored to the characteristics of PVF, based on PVF-10, including combining CNNs and Transformers, are aimed to be designed.

CRediT authorship contribution statement

Bo Wang: Writing – original draft, Data curation, Conceptualization. **Qi Chen:** Writing – review & editing, Conceptualization. **Mengmeng Wang:** Writing – review & editing, Supervision, Methodology, Funding acquisition, Conceptualization. **Yuntian Chen:** Writing – review & editing, Resources. **Zhengjia Zhang:** Writing – review & editing. **Xiuguo Liu:** Writing – review & editing. **Wei Gao:** Writing – review & editing. **Yanzhen Zhang:** Data curation. **Haoran Zhang:** Writing – review & editing, Conceptualization.

Declaration of competing interest

The authors declare that they have no known competing financial interests or personal relationships that could have appeared to influence the work reported in this paper.

Data availability

We encourage researchers in related fields to conduct meaningful studies using PVF-10, proposing advanced classification algorithms and ideal PV classification datasets. The PVF-10 and the code of experiments are available at <https://github.com/wangbobby1026/PVF-Dataset.git>.

Acknowledgements

This work was supported by the funded the National Natural Science Foundation of China (Grant 42371475, 2020J01359, 61801443 and 41801348) and the National Key Research and Development Programs of China (Grant 2016YFA0600302).

Appendix A. Supplementary data

Supplementary data to this article can be found online at <https://doi.org/10.1016/j.apenergy.2024.124187>.

References

- [1] Tang W, Yang Q, Xiong K, Yan W. Deep learning based automatic defect identification of photovoltaic module using electroluminescence images. *Sol Energy* 2020;201:453–60.
- [2] Yahya Z, Imane S, Hicham H, Ghassane A, Safia EB-I. Applied imagery pattern recognition for photovoltaic modules' inspection: a review on methods, challenges and future development. *Sustain Energy Technol Assess* 2022;52:102071.
- [3] Chen Q, et al. Remote sensing of photovoltaic scenarios: techniques, applications and future directions. *Appl Energy* 2023;333:120579.
- [4] IEA PVPS. Trends in Photovoltaic Applications. 2022 [Online]. Available: <https://iea-pvps.org/wp-content/uploads/2023/04/PVPSAnnualReport2022v7-1.pdf>.
- [5] Ramakumar R, Bigger J. Photovoltaic systems. *Proc IEEE* 1993;81(3):365–77.
- [6] Sugumaran V, et al. Fault diagnosis of visual faults in photovoltaic modules: A Review. 2021.
- [7] Ying Y, Ying P, Men H, Joo YH. Image registration based fault localization in panoramas of mountain-mounted PV plants. *Sol Energy* May 2023;256:16–31. <https://doi.org/10.1016/j.solener.2023.03.049>.
- [8] Buerhop CL, Schlegel D, Niess M, Vodermayer C, Weißmann R, Brabec CJ. Reliability of IR-imaging of PV-plants under operating conditions. *Sol Energy Mater Sol Cells* Dec. 2012;107:154–64. <https://doi.org/10.1016/j.solmat.2012.07.011>.
- [9] Buerhop C, Bommes L, Schlipf J, Pickel T, Fladung A, Peters IM. Infrared imaging of photovoltaic modules: a review of the state of the art and future challenges facing gigawatt photovoltaic power stations. *Prog Energy Sep.* 2022;4(4):042010. <https://doi.org/10.1088/2516-1083/ac890b>.
- [10] Avdelidis N, Moropoulou A. Emissivity considerations in building thermography. *Energ Buildings* 2003;35(7):663–7.
- [11] Howell JR, Mengüç MP, Daun K, Siegel R. Thermal radiation heat transfer. CRC press; 2020.
- [12] J. Kelly et al., "Challenges and best practices for deriving temperature data from an uncalibrated UAV thermal infrared camera," *Remote Sens* (Basel), vol. 11, no. 5, 2019, [Online]. Available: <https://www.mdpi.com/2072-4292/11/5/567>.
- [13] de Oliveira AKV, Aghaei M, Rüther R. Automatic inspection of photovoltaic power plants using aerial infrared thermography: a review. *Energies* 2022;15(6):2055.
- [14] Wang X, Yang W, Qin B, Wei K, Ma Y, Zhang D. Intelligent monitoring of photovoltaic panels based on infrared detection. *Energy Rep* 2022;8:5005–15.
- [15] Tsanakas JA, Ha L, Buerhop C. Faults and infrared thermographic diagnosis in operating c-Si photovoltaic modules: a review of research and future challenges. *Renew Sustain Energy Rev* 2016;62:695–709.
- [16] Pilla M, Galmiche F, Maldague XP. Thermographic inspection of cracked solar cells. In: *Thermosense XIV. SPIE*; 2002. p. 699–703.
- [17] Tanda G, Migliazzo M. Infrared thermography monitoring of solar photovoltaic systems: a comparison between UAV and aircraft remote sensing platforms. *Therm Sci Eng Prog* Feb. 2024;48:102379. <https://doi.org/10.1016/j.tsep.2023.102379>.
- [18] P. Addabbo et al., "A UAV infrared measurement approach for defect detection in photovoltaic plants," in 2017 IEEE international workshop on metrology for AeroSpace (MetroAeroSpace), IEEE, 2017, pp. 345–350.
- [19] Addabbo P, et al. UAV system for photovoltaic plant inspection. *IEEE Aerosp Electron Syst Mag* 2018;33(8):58–67.
- [20] Fernández A, et al. Robust detection, classification and localization of defects in large photovoltaic plants based on unmanned aerial vehicles and infrared thermography. *Appl Sci Jan.* 2020;10, no. 17, Art. no. 17. <https://doi.org/10.3390/app10175948>.
- [21] Alajmi M, Awedat K, Aldeeb MS, Alwagdani S. IR Thermal Image Analysis: An Efficient Algorithm for Accurate Hot-Spot Fault Detection and Localization in Solar Photovoltaic Systems. In: 2019 IEEE international conference on electro information technology (EIT); May 2019. p. 162–8. <https://doi.org/10.1109/EIT.2019.8833855>.
- [22] Bharath VS, Kurukura A Haque, Khan MA. Fault Classification for Photovoltaic modules using Thermography and Image Processing. In: 2019 IEEE Industry Applications Society Annual Meeting; Sep. 2019. p. 1–6. <https://doi.org/10.1109/IAS.2019.8912356>.
- [23] D. Kim, J. Youn, and C. Kim, "Automatic fault recognition of photovoltaic modules based on statistical analysis of uav thermography," *Int Arch Photogramm Remote Sens Spat Inf Sci*, vol. XLII-2-W6, pp. 179–182, Aug. 2017, doi: <https://doi.org/10.5194/isprs-archives-XLII-2-W6-179-2017>.
- [24] Ali MU, Khan HF, Masud M, Kallu KD, Zafar A. A machine learning framework to identify the hotspot in photovoltaic module using infrared thermography. *Sol Energy* 2020;208:643–51.
- [25] Kurukura VB, Haque A, Tripathy AK, Khan MA. Machine learning framework for photovoltaic module defect detection with infrared images. *Int J Syst Assur Eng Manag* 2022;13(4):1771–87.
- [26] Boubaker S, Kamel S, Ghazouani N, Mellit A. Assessment of machine and deep learning approaches for fault diagnosis in photovoltaic systems using infrared thermography. *Remote Sens (Basel)* 2023;15(6):1686.
- [27] Bommes L, et al. Anomaly detection in IR images of PV modules using supervised contrastive learning. *Prog Photovolt Res Appl* 2022;30(6):597–614.
- [28] Krizhevsky A, Sutskever I, Hinton GE. Imagenet classification with deep convolutional neural networks. *Adv Neural Inf Process Syst* 2012;25.
- [29] Yang R, et al. Weakly-semi supervised extraction of rooftop photovoltaics from high-resolution images based on segment anything model and class activation map. *Appl Energy* 2024;361:122964.
- [30] Zefri Y, Sebari I, Hajji H, Aniba G. Developing a deep learning-based layer-3 solution for thermal infrared large-scale photovoltaic module inspection from orthorectified big UAV imagery data. *Int J Appl Earth Obs Geoinformation* 2022;106:102652.
- [31] Kellil N, Aissat A, Mellit A. Fault diagnosis of photovoltaic modules using deep neural networks and infrared images under Algerian climatic conditions. *Energy* 2023;263:125902.
- [32] Akram MW, Li G, Jin Y, Chen X, Zhu C, Ahmad A. Automatic detection of photovoltaic module defects in infrared images with isolated and develop-model transfer deep learning. *Sol Energy* 2020;198:175–86.
- [33] Alves RHF, de Deus Junior GA, Marra EG, Lemos RP. Automatic fault classification in photovoltaic modules using convolutional neural networks. *Renew Energy* 2021;179:502–16.
- [34] Korkmaz D, Acikgoz H. An efficient fault classification method in solar photovoltaic modules using transfer learning and multi-scale convolutional neural network. *Eng Appl Artif Intel* 2022;113:104959.
- [35] Herráiz ÁH, Marugán AP, Márquez FPG. Photovoltaic plant condition monitoring using thermal images analysis by convolutional neural network-based structure. *Renew Energy* 2020;153:334–48.
- [36] Millendorf M, Obropta E, Vadhwakar N. Infrared solar module dataset for anomaly detection. *Proc. Int. Conf. Learn.*; 2020. Represent.
- [37] Alfaro-Mejía E, Loaiza-Correa H, Franco-Mejía E, Restrepo-Girón AD, Nope-Rodríguez SE. Dataset for recognition of snail trails and hot spot failures in monocrystalline Si solar panels. *Data Brief* 2019;26:104441.
- [38] Pierdicca R, Malinverni E, Piccinni F, Paolanti M, Felicetti A, Zingaretti P. Deep convolutional neural network for automatic detection of damaged photovoltaic cells. *Int Arch Photogramm Remote Sens Spat Inf Sci* 2018;42:893–900.
- [39] Bu C, Liu T, Wang T, Zhang H, Sfarra S. A CNN-architecture-based photovoltaic cell fault classification method using thermographic images. *Energies* 2023;16(9):3749.
- [40] Manno D, Cipriani G, Ciulla G, Di Dio V, Guarino S, Brano VL. Deep learning strategies for automatic fault diagnosis in photovoltaic systems by thermographic images. *Energ Convers Manage* 2021;241:114315.
- [41] Mellit A. An embedded solution for fault detection and diagnosis of photovoltaic modules using thermographic images and deep convolutional neural networks. *Eng Appl Artif Intel* 2022;116:105459.
- [42] Haidari P, Hajjahmad A, Jafari A, Nasiri A. Deep learning-based model for fault classification in solar modules using infrared images. *Sustain Energy Technol Assess* 2022;52:102110.
- [43] Dunderdale C, Brettenny W, Clohessy C, van Dyk EE. Photovoltaic defect classification through thermal infrared imaging using a machine learning approach. *Prog Photovolt Res Appl* 2020;28(3):177–88.
- [44] IEC TS 62446-3:2017. IEC Webstore. Accessed: Apr 08. [Online]. Available: <https://webstore.iec.ch/publication/28628>; 2024.
- [45] Hu Y, Cao W, Ma J, Finney SJ, Li D. Identifying PV module mismatch faults by a thermography-based temperature distribution analysis. *IEEE Trans Device Mater Reliab* 2014;14(4):951–60.
- [46] Kandeal A, et al. Infrared thermography-based condition monitoring of solar photovoltaic systems: a mini review of recent advances. *Sol Energy* 2021;223:33–43.
- [47] Fuyuki T, Kondo H, Kaji Y, Ogane A, Takahashi Y. Analytic findings in the electroluminescence characterization of crystalline silicon solar cells. *J Appl Phys* 2007;101(2).
- [48] Dhimish M. Micro cracks distribution and power degradation of polycrystalline solar cells wafer: observations constructed from the analysis of 4000 samples. *Renew Energy* 2020;145:466–77.
- [49] Mellit A, Tina GM, Kalogirou SA. Fault detection and diagnosis methods for photovoltaic systems: a review. *Renew Sustain Energy Rev* 2018;91:1–17.
- [50] He K, Zhang X, Ren S, Sun J. Deep residual learning for image recognition. In: *Proceedings of the IEEE conference on computer vision and pattern recognition*; 2016. p. 770–8.
- [51] Tan M, Le Q. Efficientnetv2: Smaller models and faster training. In: *International conference on machine learning*, PMLR; 2021. p. 10096–106.
- [52] Zhai X, Kolesnikov A, Houlsby N, Beyer L. Scaling vision transformers. *Proceedings of the IEEE/CVF Conference on Computer Vision and Pattern Recognition* 2022;12104–13.
- [53] Liu Z, et al. Swin transformer v2: Scaling up capacity and resolution. In: *Proceedings of the IEEE/CVF conference on computer vision and pattern recognition*; 2022. p. 12009–19.
- [54] Xu W, Xu Y, Chang T, Tu Z. Co-scale conv-attentional image transformers. In: *Proceedings of the IEEE/CVF international conference on computer vision*; 2021. p. 9981–90.
- [55] Ding X, Zhang X, Han J, Ding G. Scaling up your kernels to 31x31: Revisiting large kernel design in cnns. In: *Proceedings of the IEEE/CVF conference on computer vision and pattern recognition*; 2022. p. 11963–75.